Variational model with image denoising fitting term for boundary extraction of breast ultrasound images

Nurdina Badrulhisam[1]
Nurhuda Ismail[2]
Abdul Kadir Jumaat[1,3+]
Mohd Azdi Maasar[4]
Mohamed Faris Laham[5]

[1]*School of Mathematical Sciences, College of Computing, Informatics and Mathematics, Universiti Teknologi MARA, 40450 Shah Alam, Malaysia.*
[1]*Email: dinabadrul97@gmail.com*
[2]*School of Mathematical Sciences, College of Computing, Informatics and Mathematics, Universiti Teknologi MARA, Johor Branch, Pasir Gudang Campus, 81750 Johor, Malaysia.*
[2]*Email: nurhudaismail@uitm.edu.my*
[3]*Institute for Big Data Analytics and Artificial Intelligence, Kompleks Al-Khawarizmi, Universiti Teknologi MARA, 40450, Shah Alam, Selangor, Malaysia.*
[3]*Email: abdulkadir@tmsk.uitm.edu.my*
[4]*School of Mathematical Sciences, College of Computing, Informatics and Mathematics, Universiti Teknologi MARA Negeri Sembilan Branch, Seremban Campus, Malaysia.*
[4]*Email: azdimaasar@tmsk.uitm.edu.my*
[5]*Institute for Mathematical Research, Universiti Putra Malaysia, Malaysia.*
[5]*Email: mohdfaris@upm.edu.my*

(+ Corresponding author)

ABSTRACT

A variational model was used to extract or segment the breast ultrasound (BUS) image boundary in order to find a closed curve line of the abnormality region for further diagnosis. A recent selective variational model, termed the Convex Distance Selective Segmentation (CDSS) model, is effective at segmenting a specific image object. However, the CDSS model has difficulty segmenting noisy images. Unavoidable noise in BUS pictures leads to poor segmentation, as is widely recognized. The objective of this work is to propose a reformulation of the Convex Distance Selective Segmentation (CDSS) model for the purpose of segmenting BUS pictures. Consideration of four distinct image Denoising algorithms—Gaussian filter, Median filter, Wiener filter, and Rudin-Osher-Fatemi (ROF) algorithm—as the new fitting terms in the CDSS model leads to four variants of modified CDSS models called Modified CDSS based on Gaussian filter (MCDSS$_G$), Modified CDSS based on Median filter (MCDSS$_M$), Modified CDSS based on Wiener filter (MCDSS$_W$) and Modified CDSS based on ROF (MCDSS$_{ROF}$). To solve the modified models, we first derived the associate Euler-Lagrange equation and solved it in Matrix Laboratory (MATLAB) software. Experiments demonstrated that the proposed MCDSS$_{ROF}$ model based on the ROF denoising algorithm provided the highest average of Peak-Signal-To-Noise-Ratio (PSNR), Dice, and Jaccard Similarity Coefficients, indicating the highest denoising quality and segmentation accuracy in comparison to other models.

Contribution/Originality: Since noise in ultrasound images of the breast can't be avoided and makes it hard to find abnormal areas, new models are made by combining the current variational segmentation model with techniques for removing noise from images. An accurate segmentation result may help the radiologist analyze the abnormality for further diagnosis.

1. INTRODUCTION

Breast cancer is the most common cancer among women in developing countries, contributing to the second-highest number of deaths. Breast cancer is predicted to affect one out of every nine women in their lifetime [1]. Breast cancer must be detected and diagnosed early to control the disease and extend life expectancy. One of the common screening tools to detect breast cancer is ultrasound imaging. Ultrasound, also known as ultrasonography, is a technology that uses high-frequency sound waves to produce images of the inside of the body. In comparison to alternative imaging modalities, ultrasonic imaging is characterized by its non-invasive nature, absence of radiation exposure, and cost-effectiveness [2]. However, ultrasound images do have their disadvantages, such as the existence of noise [3]. This issue can lead to a misdiagnosis of the disease. To interpret medical images with higher accuracy, it is important to improve the image quality by performing image processing such as image segmentation and image denoising.

Image segmentation is the technique of partitioning an image into several segments [4]. The use of image segmentation for medical purposes is to extract the boundary of a targeted region. The extracted region will be used to analyze the types of diseases, such as cancer [5] and breast abnormalities [6-10]. One of the main obstacles in medical image segmentation is low-contrast objects [11]. In addition, extremely small objects are hard to distinguish from normal tissue [12]. Segmenting delicate areas is complex and time-consuming; nonetheless, it is possible with advances in segmentation algorithms [13]. Image segmentation allows for the direct analysis of individual items inside a picture as opposed to examining the image as a whole. This approach significantly reduces the time required for the analysis process. The process of image segmentation is accomplished by the use of several models, which may be classified into two distinct categories: non-variational and variational techniques.

The non-variational model is a category in which image segmentation processes are mostly carried out using a machine learning-based approach. Convolutional Neural Networks [14] and U-Net [15] are examples of methods used. Studies have demonstrated the efficacy of these machine learning-based techniques in non-variational image segmentation [16]. The machine learning-based technique has certain limitations, though, including being unduly dependent on the volume of data and not knowing how to segment images [17]. To get satisfactory results, a lot of data (pictures), including the label, and good processing equipment are needed; however, these things aren't always accessible. Region-growing and thresholding are two more non-machine learning-based techniques for non-variational picture segmentation. Due to their ability to segment any features or objects (including image noise) in an image, the region-growing and thresholding approaches may yield unsatisfactory results for abnormal regions with low contrast, noisy images, and close to normal tissue.

On the other hand, variational image processing views an image as a function whose sampling corresponds to the discrete matrix form of a specific picture. While a three-dimensional formulation is presented in Jumaat and Chen [18], other works on variational image segmentation algorithms in two-dimensional formulations have demonstrated that they are efficient and able to give high-quality imaging processing capabilities [19-22]. Global segmentation and selective segmentation are the two categories into which the variational model may be separated. The process of segmenting every object in the image based on specific traits is called global segmentation. Low border contrast, noisy pictures, and tissue that is close to normal, however, may result in disappointing results from the approaches. In ultrasound image segmentation research, Fang, et al. [23] and Zhao, et al. [24] formulate active contours based on local and global statistical properties of ultrasound image information. The models are effective for images with intensity inhomogeneity. However, the models developed are for a global type of segmentation, where segmenting for a particular object in the image may fail.

Selective segmentation, on the other hand, is a method of segmenting a specific object within an image. This method has a lot of potential for integration with other applications such as histopathology image processing, handwritten recognition, intensity-inhomogeneous image processing, and biometric identification. Selective segmentation is potent for BUS images because the segmentation process can be implemented directly in the breast

71

abnormality region. The selective model, namely Convex Distance Selective Segmentation (CDSS), was introduced by Spencer and Chen [22]. Another approach, which is an active contour model based on the neutrosophic theory, was introduced by Lotfollahi, et al. [25] for segmenting ultrasound images. It was found that the neutrosophic theory helps the active contour model achieve the property of selective segmentation. However, it is not guaranteed that the proposed model can segment the selected object due to the non-convexity of the formulation. On the other hand, the CDSS model by Spencer and Chen [22], which is a convex and selective model, is more reliable in segmenting a particular object in an image. However, the CDSS model may be sensitive to image noise. Therefore, some modifications to the CDSS model are needed to enhance its segmentation accuracy. In this paper, we propose to modify the CDSS model by using image denoising techniques.

Image denoising is the process of reducing the amount of noise in an image while maintaining its true image [26]. In BUS images, noise is unavoidable. A study had shown that the Wiener filter is the best model to reduce speckle-type noise compared to other filters [27]. However, Wiener filtering will blur sharp edges [26]. Linear filtering methods such as Gaussian filtering are fast but do not maintain the denoised image's key characteristics, such as having the ability to over-smooth images with a lot of noise [28], while non-linear filters are able to preserve the important aspects of the denoised image, particularly the edges. Examples of non-linear filters that can be used to reduce noise are the Median filter and total variation (TV), specifically the seminal work by Rudin, et al. [29] termed as Rudin, Osher, and Fatemi (ROF) algorithm.

Different varieties of denoising techniques can produce distinct denoising outcomes, thereby influencing the accuracy of segmentation. This study will therefore propose new selective active contour models for effectively segmenting BUS images by reformulating the CDSS model with information from the image denoising techniques: the Gaussian filter, Median filter, Wiener filter, and Rudin-Osher-Fatemi algorithm to replace the fitting term in the CDSS model. By modifying the CDSS model, we anticipate enhancements in terms of image quality and segmentation precision.

2. REVIEW OF THE RELATED MODEL

The Convex Distance Selective Segmentation (CDSS) model was created by Spencer and Chen [22] based on the piecewise constant Chan-Vese functional in Chan and Vese [21]. Assume that $z(x,y)$ is a grayscale picture. Their approach starts with the premise that the picture $z(x,y)$ is created by two significant areas. Unknown contours Γ divide the two areas. It is presumed that the region Ω_1 inside the curve or contour represents the particular item with the unknown value, c_1. The unknown value c_2 in $\Omega_2 = \Omega \backslash \Omega_1$ such that $\Omega = \Omega_1 \cup \Omega_2$ is used to estimate the picture intensity outside of the curve. $A = \{w_i = (x_i^*, y_i^*) \in \Omega, 1 \leq i \leq n_1\}$ with $n_1 (\geq 3)$ marker points will be put close to the targeted item. The normalized Euclidean distance of each point $(x,y) \in \Omega$ from its nearest point in the polygon, P such that $(x_p, y_p) \in P$, is defined as $P_d(x,y) = P_0(x,y)/\|P_0\|_{L\infty}$ and is created from the user input set A where $P_0(x,y) = \left((x - x_p)^2 + (y - y_p)^2\right)^{0.5}$. By taking the function $\phi(x,y)$ at zero level set as the segmentation curve Γ and approximating the Heaviside of $\phi(x,y)$ as $H(\phi) = 0.5\left(1 + \left(\frac{2}{\pi}\right)\arctan\left(\frac{\phi}{\varepsilon}\right)\right) \rightarrow u \in [0,1]$ for small constant ε near zero, the CDSS functional is then defined as the following Equation 1:

$$\min_{u,c_1,c_2} \{CDSS(u,c_1,c_2) = \mu \int_\Omega |\nabla u| d\Omega + \lambda \int_\Omega (z - c_1)^2 u d\Omega$$
$$-\lambda \int_\Omega (z - c_2)^2 u d\Omega + \theta \int_\Omega P_d u d\Omega + \alpha \int_\Omega v(u) d\Omega\} \tag{[1]}$$

The first term weighted by the parameter $\mu > 0$ ensures the segmented image is smooth, while the second and third terms, which are weighted by the parameter $\lambda > 0$ are the fitting terms to ensure the segmented image preserves the important geometric properties of the input image such as edge of the image. The fourth term, which is weighted by the parameter $\theta > 0$ is the distance term which will keep the evolution curve close to the targeted object. The last term is the penalty function, $v(u) = H\left(\sqrt{(2u-1)^2 + \varepsilon} - 1\right)\left[\sqrt{(2u-1)^2 + \varepsilon} - 1\right]$ which weighted by a constant

$\alpha > 0$ is introduced to ensure the solution of u is in between 0 and 1 where $H(x) = 0.5\left(1 + \left(\frac{2}{\pi}\right)\arctan\left(\frac{x}{\varepsilon}\right)\right)$. To solve the CDSS model in Equation 1, the Euler-Lagrange partial differential equation (EL-PDE) with Neumann boundary condition is derived, defined as $\mu C(u) - \lambda r - \theta P_d - \alpha v' = 0$.

Here, the curvature term $C(u) = \nabla.\left(\frac{\nabla u}{|\nabla u|}\right)$. Many gradient descent-based methods can be used to compute Equation 1. In Spencer and Chen [22] proposed using the Additive Operator Splitting scheme (AOS$_2$) to solve the equation. Although the CDSS model is effective, it may be sensitive to image noise, resulting in an unsatisfactory result in segmenting BUS images. Hence, some modifications to the CDSS model are needed to enhance its segmentation accuracy. The next section demonstrates the methodology for modifying the CDSS model by using image denoising techniques.

3. METHODOLOGY

The CDSS model will be modified by substituting the fitting term z in Equation 1 with the information from the image denoising techniques, namely the Gaussian filter, Median filter, Wiener filter, and Rudin-Osher-Fatemi (ROF) algorithm. Initially, we present the modified CDSS model based on the Gaussian filter, denoted by z_g. The modified model referred to as MCDSS$_G$ is defined by Equation 2:

$$\min_{u,c_1,c_2}\{MCDSS_G(u,c_1,c_2) = \mu \int_\Omega |\nabla u|d\Omega + \lambda \int_\Omega (z_G - c_1)^2 u d\Omega$$
$$-\lambda \int_\Omega (z_G - c_2)^2 u d\Omega + \theta \int_\Omega P_d u d\Omega + \alpha \int_\Omega v(u)d\Omega\}. \qquad [2]$$

Here, $z_G = e^{-\frac{x^2+y^2}{2\sigma^2}}$ where σ^2 is variance around each pixel (x,y).

Secondly, we define the modified CDSS model based on the Median filter, z_M. Equation 3 describes the second modified model, referred to as MCDSS$_M$:

$$\min_{u,c_1,c_2}\{MCDSS_M(u,c_1,c_2) = \mu \int_\Omega |\nabla u|d\Omega + \lambda \int_\Omega (z_M - c_1)^2 u d\Omega$$
$$-\lambda \int_\Omega (z_M - c_2)^2 u d\Omega + \theta \int_\Omega P_d u d\Omega + \alpha \int_\Omega v(u)d\Omega\}. \qquad [3]$$

Here, $z_M(x,y) = \underset{(s,t)\in S_{xy}}{median}\{z(s,t)\}$ where S_{xy} symbolize an $m \times n$ sub-image of the input noisy image, $z(s,t)$.

For the third modified model, we combine the newly generated fitting term from the Wiener filter, z_W with the CDSS model. Equation 4 describes the third modified model, referred to as MCDSS$_W$:

$$\min_{u,c_1,c_2}\{MCDSS_W(u,c_1,c_2) = \mu \int_\Omega |\nabla u|d\Omega + \lambda \int_\Omega (z_W - c_1)^2 u d\Omega$$
$$-\lambda \int_\Omega (z_W - c_2)^2 u d\Omega + \theta \int_\Omega P_d u d\Omega + \alpha \int_\Omega v(u)d\Omega\}. \qquad [4]$$

Here, $z_W = \eta + \left(\frac{\sigma^2 - v^2}{\sigma^2}\right)(z - \mu)$ where η, v^2 and σ^2 are local mean, noise variance and variance around pixel respectively.

The fourth updated model shows the insertion of the new fitting term, z_{ROF} created by the ROF model into the CDSS model. The fourth modified model termed MCDSS$_{ROF}$ is written mathematically as Equation 5:

$$\min_{u,c_1,c_2}\{MCDSS_{ROF}(u,c_1,c_2) = \mu \int_\Omega |\nabla u|d\Omega + \lambda \int_\Omega (z_{ROF} - c_1)^2 u d\Omega$$
$$-\lambda \int_\Omega (z_{ROF} - c_2)^2 u d\Omega + \theta \int_\Omega P_d u d\Omega + \alpha \int_\Omega v(u)d\Omega\}. \qquad [5]$$

Here, $z_{ROF} = z + \left(\frac{1}{2\lambda}\right)div\left(\frac{\nabla z_{ROF}}{|\nabla z_{ROF}|}\right)$.

All the modified models of Equation 2, 3, 4 and 5 are solved by solving their associated Euler-Lagrange partial differential equation (EL-PDE). Here, we demonstrate how to derive the EL-PDE for Equation 5 only because the derivation of the EL-PDE for Equation 2, 3 and 4 are mostly the same. From Equation 5, we denote that $I_1(u) = |\nabla u| = \sqrt{u_x^2 + u_y^2} = (u_x^2 + u_y^2)^{\frac{1}{2}}$, $I_2(u) = r_{ROF}u$, $I_3(u) = P_d u$, and $I_4(u) = v(u)$ where $r_{ROF} = (z_{ROF} - c_1)^2 - (z_{ROF} - c_2)^2$. Next, we define a small parameter ε which is a real parameter with a range of values around 0 and a test function ϕ. Consequently, $I_1|u + \varepsilon\phi| = |\nabla(u + \varepsilon\phi)| = \sqrt{(u_x + \varepsilon\phi_x)^2 + (u_y + \varepsilon\phi_y)^2}$. At $\varepsilon = 0$, the derivative of $\sqrt{(u_x + \varepsilon\phi_x)^2 + (u_y + \varepsilon\phi_y)^2}$ with respect to ε is given as

$$\frac{d}{d\varepsilon}\sqrt{(u_x + \varepsilon\phi_x)^2 + (u_y + \varepsilon\phi_y)^2} = \frac{1}{2}\left[u_x^2 + u_y^2\right]^{-\frac{1}{2}}.\left[2u_x\phi_x + 2u_y\phi_y\right]$$

$$= \frac{u_x\phi_x + u_y\phi_y}{\left[u_x^2 + u_y^2\right]^{\frac{1}{2}}} = \frac{\nabla u.\nabla\phi}{|\nabla u|}.$$

Reviewing the Taylor expansion as an example, consider the function $f(a) = [(x + ac_1)^2 + (y + ac_2)^2]^p$ where $p \neq 0$. The derivative with respect to a is $p[(x + ac_1)^2 + (y + ac_2)^2]^{p-1}(2(x + ac_1)c_1 + 2(y + ac_2)c_2)$. At $a = 0$, the result is $p\frac{(2xc_1 + 2yc_2)}{[x^2 + y^2]^{1-p}}$. The Taylor expansion at $a = 0$ can be defined as the following Equation 6:

$$f(a) = f(0) + f'(a)a + O(a^2) = (x^2 + y^2)^p + p\frac{(2xc_1 + 2yc_2)}{(x^2 + y^2)^{1-p}}a + O(a^2). \qquad [6]$$

Thus, by applying the Taylor expansion in Equation 6 at $\varepsilon = 0$, the term I_1 can be extended as follows.

$$I_1|u + \varepsilon\phi| = |\nabla(u + \varepsilon\phi)| = \sqrt{(u_x + \varepsilon\phi_x)^2 + (u_y + \varepsilon\phi_y)^2}$$

$$= |\nabla u| + \frac{\nabla u.\nabla\phi}{|\nabla u|}\varepsilon + O(\varepsilon^2).$$

For the second term, $I_2(u) = r_{ROF}.u$, the derivative with respect to ε and at $\varepsilon = 0$ is given as follows.

$$\frac{d}{d\varepsilon}(r_{ROF}(u + \varepsilon\phi)) = r_{ROF}\phi.$$

Thus, implementing the Taylor expansion in Equation 6 at $\varepsilon = 0$ gives,

$$r_{ROF}(u + \varepsilon\phi) = r_{ROF}u + r_{ROF}\phi\varepsilon + O(\varepsilon^2).$$

As for the third term, $I_3 = P_d.u$, the derivative with respect to ε and at $\varepsilon = 0$ is defined as

$$\frac{d}{d\varepsilon}(P_d(u + \varepsilon\phi)) = P_d\phi.$$

Hence, when applying Taylor expansion in Equation 6 at $\varepsilon = 0$, the term I_3 can be expressed as follows.

$$P_d(u + \varepsilon\phi) = P_d u + P_d\phi\varepsilon + O(\varepsilon^2).$$

Similarly, for the fourth term, $I_4(u) = v(u)$, the derivative with respect to ε and at $\varepsilon = 0$ is given as

$$\frac{d}{d\varepsilon}(v(u + \varepsilon\phi)) = v'(u)\phi.$$

Therefore, applying Taylor expansion in Equation 6 at $\varepsilon = 0$, the term I_4 becomes

$$v(u + \varepsilon\phi) = v(u) + v'(u)\phi\varepsilon + O(\varepsilon^2).$$

The next step is to determine the first variation of the functional $\text{MCDSS}_{\text{ROF}}$ with respect to u. Therefore, the first variation for $I(u) = I_1 + I_2 + I_3 + I_4$ combined with any test function ϕ will be defined as,

$$\lim_{\varepsilon \to 0}\frac{I(u + \varepsilon\phi) - I(u)}{\varepsilon}$$

$$= \int_\Omega \left[\mu\frac{\nabla u.\nabla\phi}{|\nabla u|} + \lambda r_{ROF}\phi + \theta P_d\phi + \alpha v'(u)\phi\right]d\Omega = 0.$$

74

By using Green's first identity as the following relation,

$$\int_{\Omega} \nabla\phi.\vec{\omega}\, d\Omega = \int_{d\Omega} \phi\vec{\omega}.\vec{\eta}ds - \int_{\Omega} \phi\nabla.\vec{\omega}\, d\Omega,$$

we let $\vec{\omega} = \frac{\nabla u}{|\nabla u|}$ and obtain

$$\int_{\Omega} \nabla\phi.\vec{\omega}\, d\Omega = \int_{\Omega} \nabla\phi \frac{\nabla u}{|\nabla u|}.\, d\Omega = \int_{d\Omega} \phi \frac{\nabla u}{|\nabla u|}.\vec{\eta}ds - \int_{\Omega} \phi\nabla.\frac{\nabla u}{|\nabla u|}\, d\Omega.$$

Next, set the boundary condition (Neumann Type) $\nabla u.\eta = 0$ we have,

$$\int_{\Omega}\left[-\mu\nabla.\frac{\nabla u}{|\nabla u|}\phi + \lambda r_{ROF}\phi + \theta P_d\phi + \alpha v'(u)\phi\right]d\Omega = 0.$$

The integrand is equal to zero if

$$-\mu\nabla.\frac{\nabla u}{|\nabla u|}\phi + \lambda r_{ROF}\phi + \theta P_d\phi + \alpha v'(u)\phi = 0$$
$$\Rightarrow \phi\left[-\mu\nabla.\frac{\nabla u}{|\nabla u|} + \lambda r_{ROF} + \theta P_d + \alpha v'(u)\right] = 0.$$

As a result, the EL-PDE with Neumann boundary condition for all test function ϕ for Equation 5 is defined as the following Equation 7:

$$\begin{cases} \frac{\partial u}{\partial t} = \mu\nabla.\left(\frac{\nabla u}{|\nabla u|}\right) - \lambda r_{ROF} - \theta P_d - \alpha v' = 0 & \text{in } \Omega \\ \frac{\partial u}{\partial \vec{n}} = 0 & \text{on } \partial\Omega \end{cases} \qquad [7]$$

Where $\vec{n}$ is the exterior normal at boundary of $\partial\Omega$ and $\frac{\partial u}{\partial \vec{n}}$ is the normal derivative of u at the boundary. Using a similar process, the EL-PDE for MCDSS_G, MCDSS_M and MCDSS_W defined in Equation 2, 3 and 4 respectively are defined as the following Equations 8, 9, and 10:

$$\begin{cases} \frac{\partial u}{\partial t} = \mu\nabla.\left(\frac{\nabla u}{|\nabla u|}\right) - \lambda r_G - \theta P_d - \alpha v' = 0 & \text{in } \Omega \\ \frac{\partial u}{\partial \vec{n}} = 0 & \text{on } \partial\Omega \end{cases} \qquad [8]$$

$$\begin{cases} \frac{\partial u}{\partial t} = \mu\nabla.\left(\frac{\nabla u}{|\nabla u|}\right) - \lambda r_M - \theta P_d - \alpha v' = 0 & \text{in } \Omega \\ \frac{\partial u}{\partial \vec{n}} = 0 & \text{on } \partial\Omega \end{cases} \qquad [9]$$

$$\begin{cases} \frac{\partial u}{\partial t} = \mu\nabla.\left(\frac{\nabla u}{|\nabla u|}\right) - \lambda r_W - \theta P_d - \alpha v' = 0 & \text{in } \Omega \\ \frac{\partial u}{\partial \vec{n}} = 0 & \text{on } \partial\Omega \end{cases} \qquad [10]$$

Equation 7, 8, 9 and 10 can be solved iteratively using many approaches, such as a finite difference scheme, an optimization multilevel scheme, or an operator splitting scheme. In this research, we applied the Additive Operator Splitting (AOS₂) scheme, which is similar to the method used to solve the CDSS model by Spencer and Chen [22]. Particularly in Spencer and Chen [22] and Rodtook, et al. [30] the specifics of the AOS₂ scheme are well explained.

3.1. Algorithm Steps for the Proposed Models

The algorithm below depicts the steps required to implement the new proposed models: MCDSS_G, MCDSS_M, MCDSS_W and MCDSS_{ROF}. The solutions are computed using Matrix Laboratory (MATLAB) software. To stop the program automatically, two stopping criteria were utilized. Firstly, a tolerance value $tol = 1 \times 10^{-5}$ was defined, and secondly, the maximum number of iterations, $maxit=5000$ was used. Next, we introduce Algorithm 1 as follows:

Algorithm for the proposed models:

1. Use command 'imread' in MATLAB to import BUS image.

2. Set the parameter values of α, μ, θ , λ and define the marker set A.

3. Initialize $n = 0,$ thus $u^{(0)}$.

4. **For** $iter = 1$ to maximum iterations, *maxit=5000* or $\frac{\|u^{n+1}-u^n\|}{\|u^n\|} \leq tol$ do

Calculate Equation 8 for MCDSS$_G$ model or Equation 9 for MCDSS$_M$ model or Equation 10 for MCDSS$_W$ model or Equation 7 for MCDSS$_{ROF}$ model.

5. $u \leftarrow u^{(n)}$. The final solution will be defined as the output u.

4. RESULTS AND DISCUSSION

Twenty (20) BUS pictures from Rodtook, et al. [30] were used in this investigation. Experiment 1, Experiment 2, and Experiment 3 are three different sorts of experiments that were carried out. Using the CDSS model that is currently in use as well as the updated models MCDSS$_G$, MCDSS$_M$, MCDSS$_W$, and MCDSS$_{ROF}$, we will segment 10 original BUS pictures in Experiment 1. Experiment 2 follows, showing how well each model performed in segmenting an additional 10 BUS pictures with additive noise. For both tests, the value of $\mu = 1, \alpha = 2, \lambda = 0.01$ are fixed for all problems.

The crucial parameter, which needs to be calibrated correctly, is θ. Depending on the BUS images, the value of θ varies in this study from 0.5 to 2.3. In essence, a big value of θ is required for an item that is near to tissue or picture noise, whereas a lower value of θ is required for an object that is smooth. The final Experiment 3 shows how sensitive the suggested model is to the value of the parameter θ.

Using the Jaccard Similarity Coefficient (JSC), also known as the Intersection over Union (IOU) coefficient, and the Dice Similarity Coefficient (DSC), which is defined as follows, the segmentation accuracy of all models was assessed.

$$\text{JSC} = \text{IOU} = \frac{|S_n \cap S_*|}{|S_n \cup S_*|} \times 100, \ \text{DSC} = \frac{|S_n \cap S_*|}{|S_n| + |S_*|} \times 100$$

Here S_n represents the segmented object of Ω_1 and S_* is the ground truth solution. The similarity function has a 0-100 possible return value range. Perfect segmentation quality is represented by JSC and DSC values of 100, whereas imperfect segmentation quality is represented by JSC and DSC values of 0.

In addition to JSC and DSC metrics, we use Peak-Signal-To-Noise Ratio (PSNR) to assess the denoised BUS images derived from the proposed models in Experiment 2. The PSNR is calculated using a logarithmic decibel scale and is represented by the equation shown below:

$$PSNR(X, Y) = 10.\log_{10}(255^2/MSE(X, Y))$$

Here, MSE represents the mean square error value defined by the following equation:

$$MSE(X, Y) = \frac{1}{mn} \sum_{i=1}^{i=m} \sum_{j=1}^{j=n} [X(i,j) - Y(i,j)]^2.$$

Here $X(i,j)$ the original is image and $Y(i,j)$ is the noisy or the denoised image. The higher the PSNR value, the better the denoising result.

4.1. Experiment 1

In Experiment 1, 10 original BUS images will be used as shown in Figure 1. The size of the original BUS images is 128 x 128.

All images in Figure 1 will be segmented by the existing model, CDSS, and the modified models: MCDSS$_G$, MCDSS$_M$, MCDSS$_W$ and MCDSS$_{ROF}$. For example, we illustrate two samples of segmentation results of Problem 1 and Problem 2 of Experiment 1 in Figure 2.
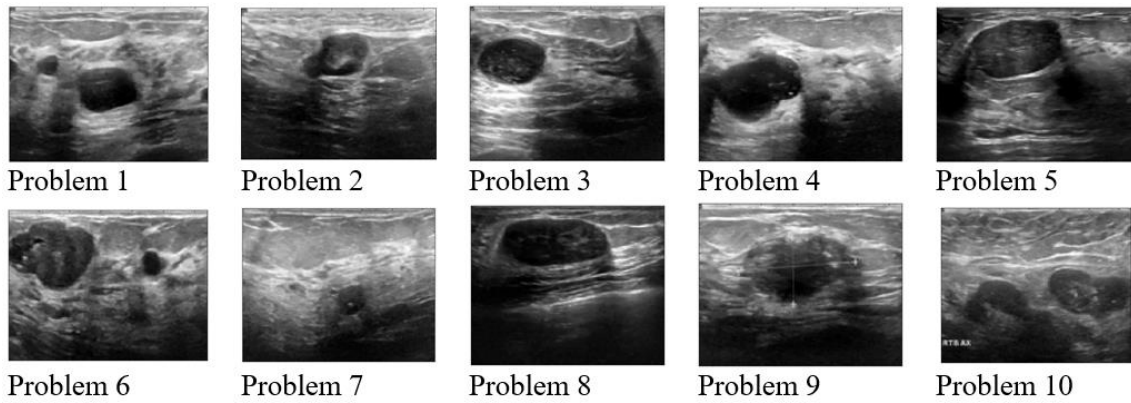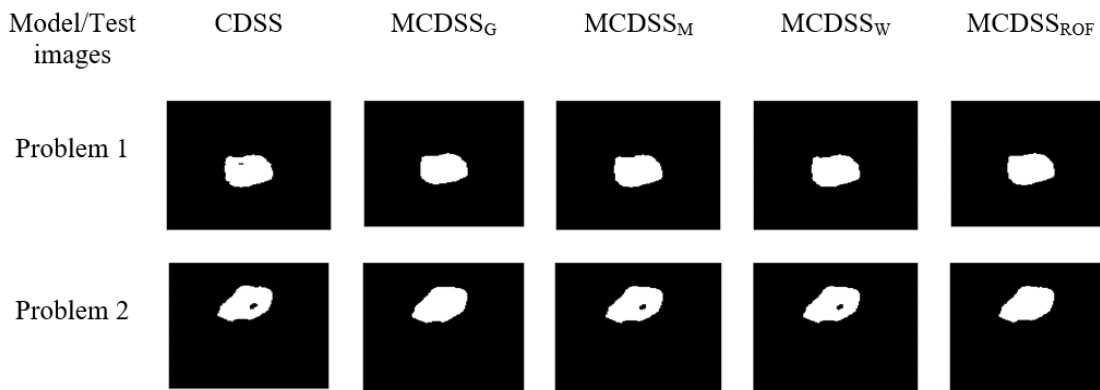
Figure 1. Test images in experiment 1.

Figure 2. Segmentation results of problem 1 and 2 of experiment 1 for all models.

The example of segmentation results shown in Figure 2 is in the form of a binary representation. For Problem 1, all of the changed models can separate out the abnormal area, except for the original model, CDSS (second column), which also separates out the noisy part inside the targeted object. For Problem 2, only two modified models are successfully segmenting the abnormal lesion without segmenting the noisy part inside the object, which are the $MCDSS_G$ (third column) and $MCDSS_{ROF}$ models (sixth column). To quantify segmentation accuracy, we compute the average of the JSC and DSC values for all test images, as shown in Figure 3.
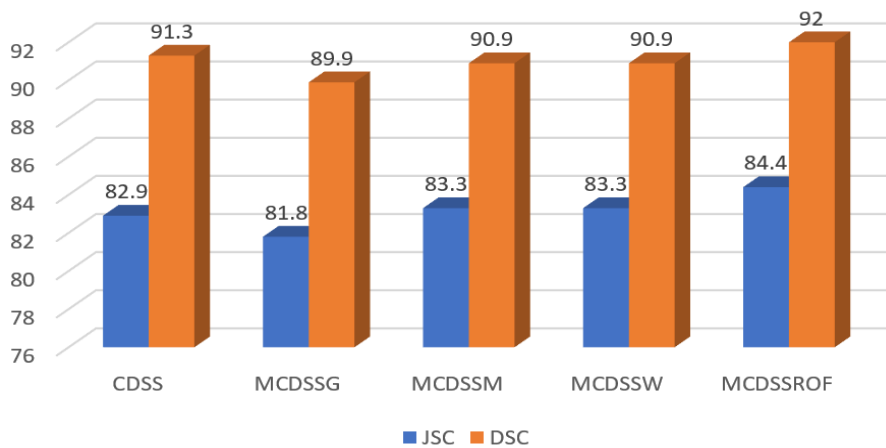
Figure 3. The Average JSC and DSC value for all test images in experiment 1.

Based on Figure 3, the $MCDSS_{ROF}$ model scored the highest average of JSC = 84.4 and DSC = 92. The lowest JSC and DSC values are obtained by the $MCDSS_G$ model, which are 81.8 and 89.9, respectively. For the CDSS model, the $MCDSS_M$ model, and the $MCDSS_W$ model, the average JSC values are 82.9, 83.3, and 83.3, respectively, while the average DSC values are 91.3, 90.9, and 90.9, respectively.

Experiment 1 indicates that the ROF model is more suitable for reducing image noise while preserving the edge of the targeted object compared to other image denoising filters applied in this study. Consequently, this helps to increase segmentation accuracy. We noticed that the weakest performance of image denoising is demonstrated by the Gaussian filter in MCDSS$_G$ model, which results in poor segmentation quality. This is mainly because the Gaussian filter will reduce the image noise but, at the same time, give a blurry effect to the object edge.

4.2. Experiment 2

To investigate the additive noise sensitivity of all models, we use another 10 BUS images corrupted with noise, as shown in Figure 4. The size of the BUS images is 128 x 128.
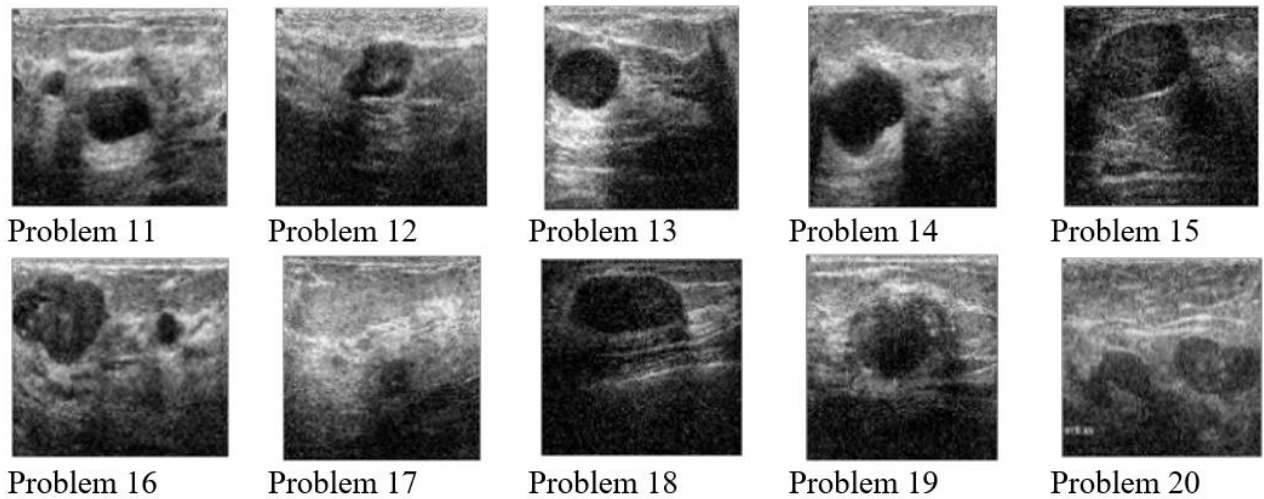
Figure 4. Test images in experiment 2.

We demonstrate two samples of segmentation results for Problems 11 and 12 using CDSS, MCDSS$_G$, MCDSS$_M$, MCDSS$_W$, and MCDSS$_{ROF}$ in Figure 5.
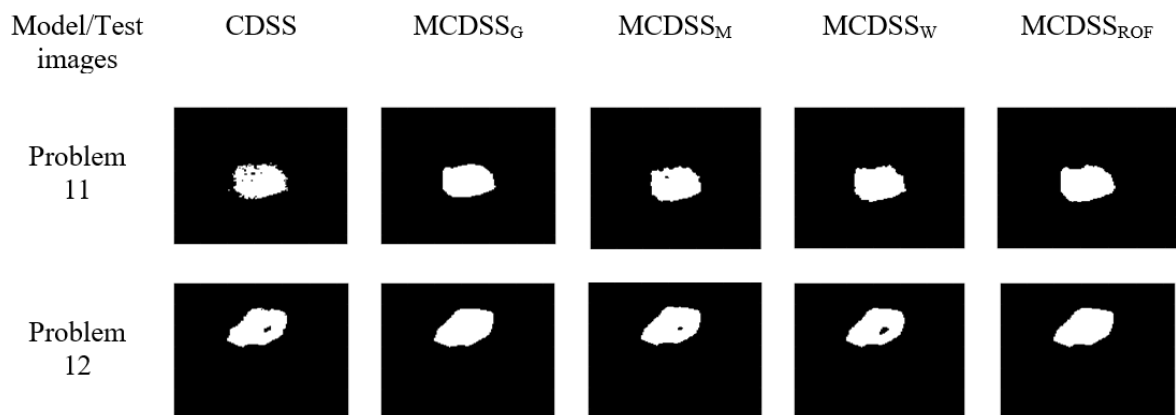

Figure 5. Segmentation results of problem 11 and 12 of experiment 2 for all models.

Figure 5 illustrates the segmentation results of Problems 11 and 12 of Experiment 2 in the form of a binary representation. The second row is the result for Problem 11, while the third row is the result for Problem 12. Based on Figure 5, all modified models can segment the abnormal lesion in Problem 11 without segmenting the noisy part inside the targeted object except for the CDSS and MCDSS$_M$ models, while for Problem 12, only MCDSS$_G$ and MCDSS$_{ROF}$ are able to segment the targeted object without segmenting the artefact inside the targeted object. To evaluate the accuracy of denoised images and segmentation accuracy quantitatively, we compute the average of PSNR, JSC, and DSC values for all 10 corrupted BUS images, as shown in the following Figure 6.
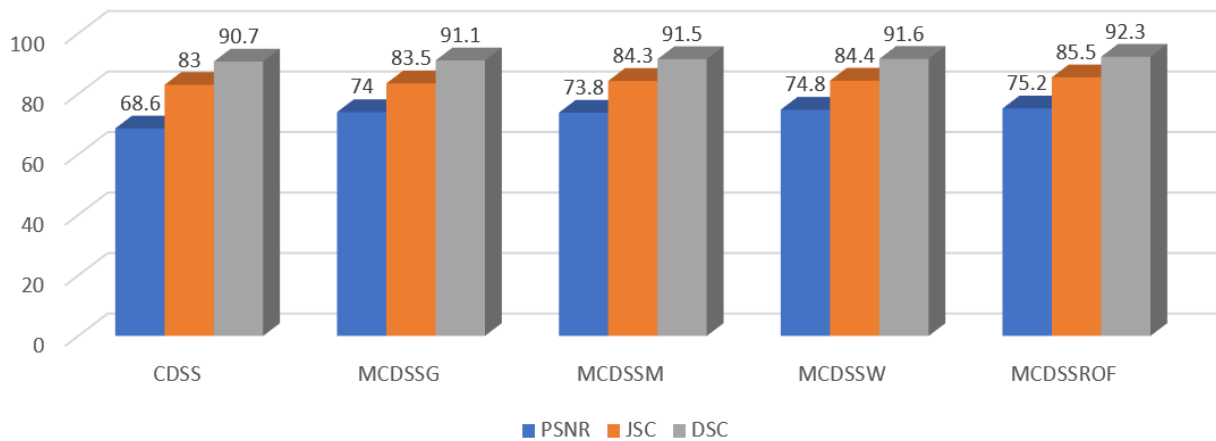
Figure 6. The average PSNR, JSC and DSC value for all test images in experiment 2.

Based on Figure 6, the average PSNR value for the MCDSS$_{ROF}$ model is the highest, at 75.2. On the other hand, the CDSS model has the lowest value of PSNR=68.6. This is mainly because there is an insufficient denoising effect in the formulation of the CDSS model. The MCDSS$_W$ model obtained the second highest value of PSNR, with an average value of 74.8. The rank of MCDSS$_G$ and MCDSS$_M$ varies based on the distorted BUS images, with an average value of 74 and 73.8, respectively.

The MCDSS$_{ROF}$ model, on the other hand, has the highest segmentation accuracy when compared to the average JSC and DSC values of 85.5 and 92.3, respectively. For most of the input images, the MCDSS$_W$ model obtained the second-highest JSC and DSC values. The MCDSS$_M$ model typically has higher JSC and DSC values than the CDSS and MCDSS$_G$ models. So, according to the results of Experiment 2, the MCDSS$_{ROF}$ model has the best denoised BUS images, which leads to the best segmentation of the corrupted BUS images.

Based on Experiments 1 and 2, the proposed MCDSSROF model is more recommended because it was able to segment the original and corrupted BUS images with the most accuracy compared to the other models used in this study.

4.3. Experiment 3

The value of θ is important in order to optimize the accuracy of the segmentation. To demonstrate the effect of parameter θ on the segmentation result, we have chosen Problem 11 from Figure 4 to be segmented by the recommended MCDSS$_{ROF}$ model. The following Figure 7 shows the segmentation results of the MCDSS$_{ROF}$ model with different values of θ for Problem 11.

Figure 7 shows the segmentation results in binary (first row) and curve (second row) form for Problem 11 using the values of $\theta = 0.1$, $\theta = 1.0$, and $\theta = 6$. By visual observation, the segmentation results clearly show that the BUS image is over-segmented when $\theta = 0.1$, where MCDSS$_{ROF}$ model unintentionally segments the healthy tissue surrounding the abnormal lesion. When $\theta = 6$, the MCDSS$_{ROF}$ model also produces an unsatisfactory result. A well-generated segment was delivered when $\theta = 1$. These visual interpretations are supported by the values of JSC and DSC, where the JSC and DSC values for the MCDSS$_{ROF}$ model with $\theta = 1$ are higher than $\theta = 0.1$ and $\theta = 6$. In conclusion, if the value of θ is too small, the model will over-segment the abnormal lesion or the healthy tissues near the abnormal lesion, and if the value of θ is too high, the boundary line of the abnormal lesion will not be segmented properly by the model.
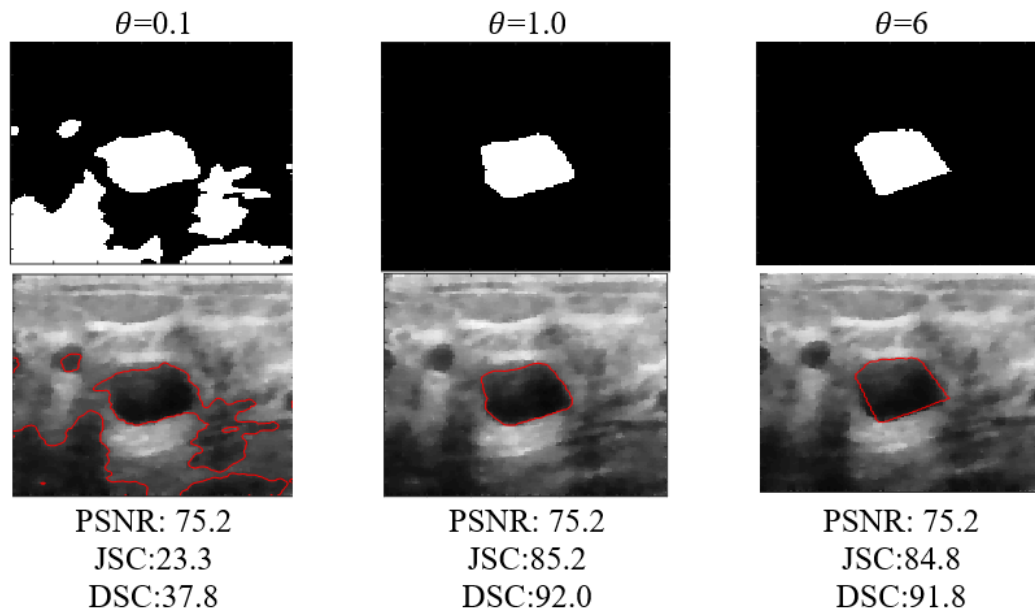
Figure 7. The segmentation results of problem 11 for MCDSS$_{ROF}$ model with different values of θ.

The limitations of the MCDSS$_{ROF}$ model can be seen in the parameter selection approach. In this model, the parameter θ was chosen by trial and error to achieve good segmentation results, which is difficult and time-consuming.

5. CONCLUSION

The focus of this research is to extract or segment the abnormality region in BUS images using a variational selective segmentation model. Due to the limitations of the existing model, CDSS, in handling images with noise, this research proposed four modified versions of the model: MCDSS$_G$, MCDSS$_M$, MCDSS$_W$, and MCDSS$_{ROF}$. The modification involved adding the image denoising algorithm as the appropriate fitting term in the formulation.

To solve the modified models, we first provide the Euler-Lagrange partial differential equation for each modified model. There are numerous iterative methods for solving the Euler-Lagrange partial differential equations. In this study, we have suggested solving the problems using Additive Operator Splitting (AOS$_2$) scheme. Two experiments were conducted in order to compare the performances of the original and modified models. The first experiment was to segment the original BUS images, while the second experiment was to segment the corrupted BUS image with additive noise. The numerical performances of the original and modified models were analyzed using PSNR, JSC, and DSC. The PSNR was used to evaluate the quality of the denoised BUS images, while the JSC and DSC were used to evaluate the segmentation accuracy.

From the two experiments carried out, the JSC and DSC values showed that the accuracy of segmentation was better in most of the modified models than in the original model, CDSS, except for MCDSS$_G$. The quality of the denoised BUS image, as indicated by PSNR value from all modified models, is higher than the original BUS images. The lowest quality of the BUS image was obtained by the CDSS model. Results demonstrated that the MCDSS$_{ROF}$ produced a better quality denoised BUS image, and consequently, the segmentation accuracy was higher compared to other models. The final experiment demonstrated the sensitivity of the recommended MCDSS$_{ROF}$ model towards different values of parameter θ where an appropriate value of θ is needed to acquire a better segmentation result. In the future, the MCDSS$_{ROF}$ model can be extended to the color domain and 3-D formulation.

REFERENCES

[1] American Cancer Society, "Breast cancer facts & figures 2019-2020," Retrieved: https://www.cancer.org/content/dam/cancer-org/research/cancer-facts-and-statistics/breast-cancer-facts-and-figures/breast-cancer-facts-and-figures-2019-2020.pdf. [Accessed May 22, 2022], 2019.

[2] Center for Devices and Radiological Health, "Ultrasound imaging," Retrieved: https://www.fda.gov/radiation-emitting-products/medical-imaging/ultrasound-imaging. [Accessed May 22, 2022], 2020.

[3] M. Gupta, H. Taneja, and L. Chand, "Performance enhancement and analysis of filters in ultrasound image denoising," *Procedia Computer Science*, vol. 132, pp. 643-652, 2018. https://doi.org/10.1016/j.procs.2018.05.063

[4] Y. Tan, *Applications. In GPU-based parallel implementation of swarm intelligence algorithms.* Amsterdam: Elsevier Inc., 2016.

[5] S. N. Kumar, A. L. Fred, H. A. Kumar, and P. S. Varghese, *Performance metric evaluation of segmentation algorithms for gold standard medical images. In: Sa, P., Bakshi, S., Hatzilygeroudis, I., Sahoo, M. (Eds.), Recent Findings in Intelligent Computing Techniques. Advances in Intelligent Systems and Computing.* Singapore: Springer, 2018.

[6] A. K. Jumaat, W. E. Z. W. A. Rahman, A. Ibrahim, and R. Mahmud, "Segmentation and characterization of masses in breast ultrasound images using active contour," presented at the 2011 IEEE International Conference on Signal and Image Processing Applications (ICSIPA), 2011.

[7] S. S. Yasiran *et al.*, "Comparison between GVF snake and ED snake in segmenting microcalcifications," in *2011 IEEE International Conference on Computer Applications and Industrial Electronics (ICCAIE)*, 2011: IEEE, pp. 597-601.

[8] A. K. Jumaat, W. E. Rahman, A. Ibrahim, S. S. Yasiran, R. Mahmud, and A. A. Malek, "Masses characterization based on angular margin measurement," in *2012 Fourth International Conference on Computational Intelligence, Modelling and Simulation*, 2012: IEEE, pp. 265-269.

[9] S. S. Yasiran *et al.*, "Microcalcifications segmentation using three edge detection techniques," in *2012 IEEE International Conference on Electronics Design, Systems and Applications (ICEDSA)*, 2012: IEEE, pp. 207-211.

[10] A. K. Jumaat *et al.*, "Performance comparison of Canny and Sobel edge detectors on Balloon Snake in segmenting masses," in *2014 International Conference on Computer and Information Sciences (ICCOINS)*, 2014: IEEE, pp. 1-5.

[11] S. V. M. Sagheer and S. N. George, "A review on medical image denoising algorithms," *Biomedical Signal Processing and Control*, vol. 61, p. 102036, 2020. https://doi.org/10.1016/j.bspc.2020.102036

[12] A. M. Aravanis, M. Lee, and R. D. Klausner, "Next-generation sequencing of circulating tumor DNA for early cancer detection," *Cell*, vol. 168, no. 4, pp. 571-574, 2017. https://doi.org/10.1016/j.cell.2017.01.030

[13] A. S. Dar and D. Padha, "Medical image segmentation: A review of recent techniques, advancements and a comprehensive comparison," *International Journal of Computer Sciences and Engineering*, vol. 7, no. 7, pp. 114-124, 2019. https://doi.org/10.26438/ijcse/v7i7.114124

[14] W. K. Moon, Y.-W. Lee, H.-H. Ke, S. H. Lee, C.-S. Huang, and R.-F. Chang, "Computer-aided diagnosis of breast ultrasound images using ensemble learning from convolutional neural networks," *Computer Methods and Programs in Biomedicine*, vol. 190, p. 105361, 2020. https://doi.org/10.1016/j.cmpb.2020.105361

81

[15] M. Amiri, R. Brooks, B. Behboodi, and H. Rivaz, "Two-stage ultrasound image segmentation using U-Net and test time augmentation," *International Journal of Computer Assisted Radiology and Surgery,* vol. 15, no. 6, pp. 981-988, 2020. https://doi.org/10.1007/s11548-020-02158-3

[16] S. Masood, M. Sharif, A. Masood, M. Yasmin, and M. Raza, "A survey on medical image segmentation," *Current Medical Imaging,* vol. 11, no. 1, pp. 3-14, 2015.

[17] L. K. Lee, S. C. Liew, and W. J. Thong, "A review of image segmentation methodologies in medical image," in *Advanced Computer and Communication Engineering Technology: Proceedings of the 1st International Conference on Communication and Computer Engineering,* 2015: Springer, pp. 1069-1080.

[18] A. Jumaat and K. Chen, "Three-dimensional convex and selective variational image segmentation model," *Malaysian Journal of Mathematical Sciences,* vol. 14, no. 3, pp. 437-450, 2020.

[19] A. K. Jumaat and K. Chen, "A reformulated convex and selective variational image segmentation model and its fast multilevel algorithm," *Numerical Mathematics Theory Methods and Applications,* vol. 12, no. 2, pp. 403-437, 2018. https://doi.org/10.4208/nmtma.oa-2017-0143

[20] A. K. Jumaat and K. Chen, "An optimization-based multilevel algorithm for variational image segmentation models," *Electronic Transactions on Numerical Analysis,* vol. 46, pp. 474–504, 2017.

[21] T. F. Chan and L. A. Vese, "Active contours without edges," *IEEE Transactions on Image Processing,* vol. 10, no. 2, pp. 266-277, 2001. https://doi.org/10.1109/83.902291

[22] J. Spencer and K. Chen, "A convex and selective variational model for image segmentation," *Communications in Mathematical Sciences,* vol. 13, no. 6, pp. 1453-1472, 2015. https://doi.org/10.4310/cms.2015.v13.n6.a5

[23] L. Fang, T. Qiu, Y. Liu, and C. Chen, "Active contour model driven by global and local intensity information for ultrasound image segmentation," *Computers & Mathematics with Applications,* vol. 75, no. 12, pp. 4286-4299, 2018. https://doi.org/10.1016/j.camwa.2018.03.029

[24] W. Zhao, X. Xu, Y. Zhu, and F. Xu, "Active contour model based on local and global Gaussian fitting energy for medical image segmentation," *Optik,* vol. 158, pp. 1160-1169, 2018. https://doi.org/10.1016/j.ijleo.2018.01.004

[25] M. Lotfollahi, M. Gity, J. Y. Ye, and A. Mahlooji Far, "Segmentation of breast ultrasound images based on active contours using neutrosophic theory," *Journal of Medical Ultrasonics,* vol. 45, no. 2, pp. 205-212, 2018. https://doi.org/10.1007/s10396-017-0811-8

[26] L. Fan, F. Zhang, H. Fan, and C. Zhang, "Brief review of image denoising techniques," *Visual Computing for Industry, Biomedicine, and Art,* vol. 2, no. 1, pp. 1-12, 2019. https://doi.org/10.1186/s42492-019-0016-7

[27] N. Kumar and M. Nachamai, "Noise removal and filtering techniques used in medical images," *Oriental Journal of Computer Science and Technology,* vol. 10, no. 1, pp. 103-113, 2017. https://doi.org/10.13005/ojcst/10.01.14

[28] K. S. Rani and D. N. Rao, "A comparative study of various noise removal techniques using filters," *Research & Reviews: Journal of Engineering and Technology,* vol. 7, no. 2, pp. 47-52, 2018.

[29] L. I. Rudin, S. Osher, and E. Fatemi, "Nonlinear total variation based noise removal algorithms," *Physica D: Nonlinear Phenomena,* vol. 60, no. 1-4, pp. 259-268, 1992. https://doi.org/10.1016/0167-2789(92)90242-f

[30] A. Rodtook, K. Kirimasthong, W. Lohitvisate, and S. S. Makhanov, "Automatic initialization of active contours and level set method in ultrasound images of breast abnormalities," *Pattern Recognition,* vol. 79, pp. 172-182, 2018. https://doi.org/10.1016/j.patcog.2018.01.032